Precipitation behavior of Al-Si-Cu-Mg(-Fe) alloys by a deformation-semisolid extrusion process

DaeHan Kim[1], JaeHwang Kim[2,*] Sigurd Wenner[3,4], Elisabeth Thronsen[4], Calin Daniel Marioara[3], Randi Holmestad[4], Equo Kobayashi1[1]

[1]*Department of Materials Science and Engineering, Tokyo Institute of Technology, 2-12-1-S8-18 Ookayama, Meguro-ku, Tokyo, Japan, 152-8552*

[2]*Carbon and Light Materials Application Group, Korea Institute of Industrial Technology, 222 Palbok-ro, Jeonju-si, South Korea, 54896*

[3]*SINTEF Industry, N-7465 Trondheim, Norway*

[4]*Department of Physics, Norwegian University of Science and Technology (NTNU), N-7491 Trondheim, Norway*

*Corresponding author at: Korea Institute of Industrial Technology, Carbon and Light Materials Application Group, 222 Palbok-ro, Jeonju-si, South Korea, 54896

E-mail address: raykim@kitech.ac.kr

Abstract

Al-4.5Si-1Cu-0.3Mg(-1Fe) (wt.%) alloys fabricated by a deformation-semisolid extrusion (D-SSE) process have been investigated by transmission electron microscopy, down to the atomic level. T5 and T6 heat treatments were conducted to understand the age-hardening behavior of the alloys. Disordered Mg-Si(-Cu) precipitates with strong Cu enrichments at their interfaces with the Al matrix have been observed in the overaged conditions of both heat treatments and in the peak hardness of the T6 condition, but only Cu-containing atomic clusters were detected in the peak hardness of the T5 heat treatment. Despite having a lower bulk precipitate number density at comparable precipitate size and volume fraction, hardness in the T6 condition was higher in the alloy with highest Fe content due to the extra contribution from the precipitates nucleated on fragmented β-Al_5FeSi particles and grain boundaries. Many of these precipitates were Q'-phase, and two new coherent interfaces with the Al matrix are reported for this phase.

Keywords: hybrid precipitates, grain boundary precipitates, Fe-intermetallic compounds, Al-Si-Cu-Mg(-Fe) alloys.

1. Introduction

Aluminum alloys are often used as automotive and structural components due to light weight, specific strength and formability. Fe is introduced to aluminum alloy from scraps, secondary ingots, and during recycling and processing. Various Fe-IMCs (Fe-intermetallic compounds) i.e. α-, β- and π-AlFeSi particles appear when Fe is introduced to Al-Si alloys [1-2]. They are detrimental to the ductility acting as crack-initiating sites and paths [3].

Recently, the negative effect of Fe-IMCs on the mechanical properties has been reduced by deformation-semisolid forming (D-SSF) and caliber rolling processes [4-6]. The D-SSF process is an effective method for breaking Fe-IMCs and inducing large strain in the Al matrix. Since Fe is introduced during recycling, it is important to control the irregular-shaped Fe-IMCs and to optimize the mechanical properties of high Fe-containing alloys. Further enhancement of the mechanical properties in high Fe-containing alloys can be obtained by the formation of precipitates through a post heat treatment.

Al-Si based alloys are used for casting and do not require heat treatments. However, precipitates can nucleate during aging if solute elements such as Mg, Si, and Cu are added. For example, those elements are added to enhance the strength by precipitate hardening in A319 (Al-Si-Cu-Mg) and A356 (Al-Si-Mg) cast alloys. The alloys studied in the present work have composition Al-4.5Si-1Cu-0.3Mg(-1Fe) (wt%) and are considered heat treatable. By adding elements such as Mg, Si and Cu to pure Al, metastable precipitates nucleate during heat treatments at elevated temperature. The precipitates are favorable for strength and different types can nucleate depending on the composition of the alloy and thermomechanical treatment [7]. The precipitation sequence of Al-Cu alloys is usually given as follows [8]:

super saturated solid solution (SSSS) → atomic clusters → Guinier-Preston (GP) 1 zone → GP2 zone (θ'') → θ'→ θ. The precipitation sequence of Al-Mg-Si-Cu alloy is summarized as follows [9-10]:

SSSS→ atomic clusters → GP zones → β'', L, QP, QC → β', Q' → β, Q.

The GP1 zone in the Al-Cu system is actually an enriched {200}Al plane [8, 11] and will be referred to as either 'GP zone' or 'enriched {200}Al plane', or 'Cu wall' in this paper. The GP2 zone is also called θ'' and consists of two enriched {200}Al planes separated by $4dAl_{200}$ [12].

The kinetics of precipitation is accelerated by increasing Cu content in Al-Mg-Si-Cu alloys [13]. Moreover, Cu additions to the Al-Mg-Si system enable nucleation of complex and interesting precipitates. The number density of the metastable β'' phase gradually decreases while the occurrence of Q', S, L and θ' phases increases with increasing Cu content [14]. A high amount of Cu addition (~4.5 wt%) causes the hardness to decrease more rapidly as compared to corresponding Cu-free alloys during over-aging [13].

Gazizov et al. [15] have investigated the precipitation behavior of an Al-4.9Cu-0.74Mg-0.51Si-0.48Mn-0.1Cr-0.08Ti-0.02Fe alloy. The terms of ‘Cu capsule’ and ‘hybrid precipitate’ are introduced to clarify the crystal structure of the precipitates. A ‘Cu capsule’ refers to a Mg-Si(-Cu) needle-type precipitate with Cu enrichment at all interfaces as viewed along the needle-length, giving the appearance of a tube, encapsulating precipitate. ‘Hybrid precipitates’ are defined as needle or lath type disordered precipitates containing structural units of known precipitates from both the Al-Mg-Si-Cu and Al-Cu systems. Wenner et al. [16] studied the precipitation formed during the artificial aging of an aluminum alloy containing Zn, Cu, Mg and Si. Combinations of disordered Al-Mg-Si-Cu phases as well as S and θ' were found. These studies have used the high-angle annular dark-field scanning transmission electron microscopy (HAADF-STEM) technique, which provides Z-contrast spatial atomic resolution that enables the investigation of precipitate atomic arrangement in great details [17-19].

In the present study, two Al-Si- cast alloys containing approximately the same amount of Si, Cu and Mg and different amount of Fe are studied for developing recycled aluminum alloys using a deformation-semisolid extrusion (D-SSE) process [4]. Low Fe content is required to improve the ductility of aluminum alloys, while a high mount of Fe (~1 %) is purposefully added to form Fe-IMCs. A high Fe-containing aluminum alloys have been neglected for studying structural analysis of precipitates since Fe-IMCs are detrimental to the mechanical properties and lifetime of materials. A high strength and ductile aluminum alloys containing Fe contents would be feasible using a D-SSE process and post heat treatments. Cost saving and recycled resources will be followed. T5 and T6 heat treatments are considered in this study to control the precipitation behavior and the balance between strength and ductility. The formation and kinetics of precipitates are also affected by the cooling rates from solution heat treatment (SHT) before natural- and artificial aging (NA and AA). Meanwhile, the role of Fe-IMCs on the formation of nano-sized precipitates has not been fully documented and the crystal structures of hybrid precipitates containing Cu have not been fully understood. Therefore, the aim of the present study is to investigate the precipitation behavior of Al-4.5Si-1Cu-0.3Mg(-1Fe) alloys produced by a D-SSE process. We focus on precipitate statistics and the atomic structure of hybrid precipitates using atomic resolution HAADF-STEM. As all the metastable precipitates in the Al-Mg-Si(-Cu) and Al-Cu system have plate/needle/lath morphologies with the main growth direction along <100>Al, all the TEM investigations shown in this work were performed with the Al matrix in this orientation.

2. Experiment procedure

Chemical compositions of the two Al-Si based alloys are given in Table 1. From now on the two alloy compositions are termed ‘0.2 Fe and 1 Fe’. The alloys were cast and homogenized at 520 °C for 24 h. The D-SSE process, which is a combination of deformation and a semi-solid extrusion process, was conducted to uniformly fragment the Fe-IMCs. 50% of deformation at 350 °C was applied to samples with a dimension of 20 x 30 x 40 mm^3. The samples were heated to a semi-solid temperature (~555 °C) and cylinder type samples with a radius of 4 mm were produced by the semi-solid extrusion process. The extrusion ratio was 40:1 and the ram speed was 0.5 mm / sec. The extruded profiles were stored at room temperature for approximately six months. T5 (AA at 170 °C without SHT) and T6 (AA at 170 °C with SHT at 520 °C for 2 h followed by water quenching) treatments were carried out. Vickers hardness testing was performed using a load of 200 g and a dwell time of 15 s. At least five indentations were acquired on each sample to obtain an average value of hardness.

TEM samples were made by polishing to less than 100 μm thickness and punching out 3 mm discs. A mixture of 2/3 methanol and 1/3 nitric acid was used for electropolishing. The electrolyte was cooled down to a temperature lower than -25 °C and a voltage of 20 V was used. A JEOL JEM-2100 operated at 200 kV, equipped with a GIF-2000 Electron energy loss spectroscopy (EELS) spectrometer, was used for bright-filed (BF) TEM imaging of the precipitate microstructure. The area of precipitates is estimated using Image-J software based on the cross section of precipitates pointing in the viewing direction. 6 TEM images corresponding to approximately 1000 precipitate cross sections were acquired. TEM images were filtered by band pass and precipitates with a circularity from 0.7 to 1.0 were selected to increase accuracy of the quantification. The statistics were obtained from the Al matrix away from regions with grain boundaries (GBs) and β-Al_5FeSi particles. The number, cross-section area and length of precipitates including the thickness of TEM samples were used to estimate the volume fraction of the precipitates. The full statistical approach can be found from the previous studies [20-21]. The thickness of the specimen is estimated from EELS measurements. EELS has become a common technique for measuring the thickness of an electron-transparent specimen, which is required for the estimation of precipitate number density by TEM imaging. The thickness, t is given by the ratio of the total intensity in the EELS spectrum to the total intensity of the zero-loss spectrum $ln\ (I_t/I_0)$ as [22],

$$t = \lambda \ ln\ (I_t / I_o) \qquad (1)$$

where λ represents the inelastic mean free path (IMFP) in the aluminum alloy. The value of the IMFP (λ_{exp}) used in this work is 143 nm [23].

An image and probe Cs-corrected JEOL ARM-200F cold FEG microscope operated at 200 kV was employed for HAADF-STEM imaging. The samples were plasma-cleaned to remove contaminations using a Fishione 1020 plasma cleaner before they were inserted into the TEM. The probe size was 0.08 nm, the convergence semi-angle was 27 mrad and the inner and outer collection angles were 42 and 178 mrad, respectively. Some images are slightly distorted due to specimen drift during acquisition. HAADF-STEM images are filtered unless otherwise specified. A circular band pass mask is applied on the FFTs and inverse FFTs (IFFTs) were performed on the masked area, suppressing all features with separation shorter than 0.15 nm in real space. It is noted that

0.15 nm is close to the minimum projected atomic column separation for precipitates in the Al-Mg-Si(-Cu) system viewed along their needle lengths.

3. Results and discussions

3.1 Age-hardening of T6 heat-treated alloys

Fig. 1 (a) shows the age-hardening curves of T5 and T6 heat-treated 0.2 Fe and 1 Fe alloys. The arrows indicate which samples were selected for TEM observations. Hardness values of Al-Si alloys increase with alloying elements [24]. Hardness of Fe-IMC is higher than the primary aluminum in Al-Si alloys [25]. Namely, the formation of Fe-IMCs is contributed to an increase in hardness. Hardness of 1 Fe is slightly higher than 0.2 Fe right after solution heat treatment in Fig. 1 (a) (green and blue lines), indicating the difference of Fe contents. The higher HV in 1 Fe is not only be attributed to the precipitation sequence and precipitates, but also related to the fragmented Fe-IMCs. Micrographs of as-extruded 0.2 and 1 Fe alloys before aging are presented as shown in Fig. 2. Si and Fe-IMCs are marked by yellow arrows, respectively. A high number density of Fe-IMCs is identified in case of 1 Fe (Fig. 2 (b)).

The precipitation kinetics was accelerated for the conditions T6 by rapid cooling from SHT while relatively broad aging curves were identified in the T5 treated alloys. The hardness difference of T5 and T6 treated 1 Fe alloys is as shown in Fig. 1 (b). The hardness difference is calculated based on the difference between the hardness values of the aged sample and the as-quenched (for T6) or as-extruded (for T5) ones. The slope of the aging curves is connected to the kinetics of clustering (up to 2 *ks*) and precipitation. It is observed that the hardness obtained from precipitates during AA increases with SHT. The hardness of T5 and T6 1 Fe alloys are comparable at the peak aging stage.

Fig. 3 shows bright-field TEM images of the T6 treated alloys after aging for 6 and 72 h. Nano-sized needle and lath precipitates in the bulk oriented along the <001>Al zone axis are observed in both 0.2 Fe and 1 Fe alloys. A slightly higher number density of precipitates is measured in the 0.2 Fe alloy aged for 6 h compared to that of 1 Fe. The average needle lengths of precipitates in 0.2 Fe and 1 Fe alloys are very short, 16.2 and 13.3 nm, respectively. The average precipitate cross sections in 0.2 Fe and 1 Fe alloys are 2.9 and 3.3 nm^2, respectively. This gives a higher precipitate volume fraction in the 0.2 Fe alloy aged for 6 h. The full statistical results of precipitates on the matrix are given in Table 2. It is observed that T6 treated 1 Fe alloy aged for 6 h has lower precipitate number densities than the 0.2 Fe alloy since solute Si content consumed to form the Fe-IMCs with Fe and Al in the 1 Fe. ~~at comparable precipitate sizes and volume fractions.~~ Thus, the strength contribution from bulk hardening precipitates should be lower in this alloy. However, Fig. 1 (a) shows that 1 Fe alloy is harder than 0.2 Fe, implying the existence of additional strength contributions. The Q' phase on grain boundaries and β-Al_5FeSi (which are not included in the numbers) contribute to the higher hardness than that of 0.2 Fe.

Figures 4 and 5 show high-resolution HAADF-STEM images of precipitates in the T6 treated 0.2 Fe and 1 Fe alloys aged for 6 h. The L phase, incorporating local symmetries of the C phase [9], GP like structure [8, 15] and Guinier-Preston-Bagaryastsky (GPB) zone [26-27] is shown in Fig. 3 (a). Although the L phase is disordered, the precipitates sometimes have mirror and/or rotation symmetries [28], as exemplified by the mirror plane marked by a dotted line in Fig, 4 (a). Both GP like structures and incomplete GPB zone units from the Al-Cu and Al-Cu-Mg systems were identified [8, 15, 26-27]. A hybrid β'' phase mixed with a GP like structure is shown in Fig. 4 (b). The GP-like structure, or 'Cu wall' is located at the left side of the particle. The 'eye' is the building block of β'', which can be stacked in various ways [29-31]. Two terms β2'' and β3'' were found by previous works [29-31]. Different β'' variants are overlaid as shown in Fig 4 (c). A half monoclinic β'' unit at the upper side, β_2'' in the middle, β_3'' at the lowest, and another incomplete (only 3 eyes) β'' at the low-left side can be identified in Fig. 4 (b). Some Cu columns, which have higher atomic number than Al, Mg and Si, and thus appear bright, are found at certain sites in the β'' phase.

In the 1 Fe alloy, a Cu capsule (middle), Cu walls (upper right) and β'' (lower right) are shown in Fig 5. (a). The Cu capsule type [15] refer to Mg-Si-Cu precipitates with high coherency with the Al matrix that are encapsulated by Cu-enriched {200}Al planes (GP-like structures). The Cu walls precipitate refers to a new type found by Marioara et al. [12] that contains a Mg-Si core delimited by two Cu walls (enriched {200}Al planes) separated by 6d Al_{200}. In addition, a precipitate consisting of a fragment of β'', segregated Cu atoms at the interfaces and a GP like structure, was observed as shown in Fig. 5 (b). All these precipitates can be classified as hybrids because they incorporate structural elements from the precipitates formed in the Al-Mg-Si(-Cu) and Al-Cu systems.

In the following, we focus on details in the 1 Fe alloy to investigate the crystal structure of the hybrid precipitates. HAADF-STEM images of the T6 treated 1 Fe alloy aged for 72 h are presented in Fig. 6. In (a-b), two Q' phases surrounded by GP like structures are shown. A disordered precipitate containing local Cu sub-unit clusters (the building blocks of Q' and C phases [28]) and units isostructural with the stacking fault reported in [12] is observed in Fig. 5 (c). A β'' phase with Cu-enriched interfaces in (d), L phase with a disordered structure in (e) and the L phase containing fragments of C and Q' phases in (f) are clearly identified. It seems like the Cu columns are systematically ordered in all types of precipitates as they grow during aging. Apart from Cu sites in the C and Q' structures, they tend to position at the vicinity of the interfaces between precipitates and matrix.

3.2 Q' phase on β-Al_5FeSi particles and grain boundaries

Fe-containing particles are known as impurities in aluminum alloys. The nucleation of α- and β-AlFeSi particles is determined by chemical composition and heat treatment. Lervik et al. [32] have reported that β-Mg_2Si and η-$MgZn_2$ were nucleated on AlFeSi particles in an AA 7003 alloy. Only β-Al_5FeSi particles were detected in the 1 Fe alloy owing to the high amount of Si and Fe contents [33] and the ratio of Fe/Si was found to be approximately 1:1 by EDS analysis. In this alloy, the Q' phase has been found to nucleate on β-Al_5FeSi particles. One example is shown in Fig. 7 (a-c). It is noted that β-Al_5FeSi particles are thermally stable at elevated temperature, and act as nucleation sites for precipitates. HAADF-STEM images in Fig 7 (d-f) zoom on the Q' phases nucleated on the β-Al_5FeSi particle. Coherent (along <510>Al) and irregular interfaces between the Q' and the Al matrix are shown in Fig. 7 (e) and (f), respectively. It is interesting to notice that Cu atoms positioned at the coherent interface have a triangle-shaped feature, which has not been reported before. This atomic arrangement is also sporadically observed at the interface of the particle in Fig. 7 (f).

In addition, the Q' phase nucleates at grain boundaries, either during the cooling after extrusion or during artificial aging. A Q' phase with different interfaces is shown in Fig. 8. The interfaces with Al of the left [001]Al oriented grain and the right grain with unknown orientation are different. An example of periodic arrangement of Cu atomic columns at the interface between the precipitates and the matrix, is identified in Fig. 8 (b) [12, 31]. It consists of short Cu walls (enriched {200}Al planes viewed edge-on) with 1.04 nm periodicity along <510>Al. It should be noted that this interface is very different from a regular Q' <510>Al interface [12] and from the interface of the Q' phase nucleated on the β-Al_5FeSi particle and presented in Fig. 7 (e). The coherent interfaces with atomic overlay along <510>Al of the Q' precipitates from [12], from Fig. 7 (e) and Fig. 8 (b) are presented in Fig. 9. The overlay is based on the construction rules for precipitates in Al-Mg-Cu and Al-Mg-Si(-Cu) alloys published in [30], and on the Z-contrast of atomic columns provided by the HAADF-STEM images. In the case of the normal interface (Fig. 9 (a)), the connection between Q' and Al matrix along <510>Al is done directly, as the Q' unit cells have direct contact with the Al matrix. However, in the case of the Q' nucleated at the β-Al_5FeSi (Fig. 9 (b)) and of the Q' nucleated on the GB (Fig. 8 (c)), the connection between Q' unit cells and the Al matrix is done through the insertion of Cu-rich buffer layers. One layer is in the form of GP-like units (Cu walls) in the case of the Q' nucleated at the GB, and another as a more triangular atomic arrangement in the case of Q' nucleated on the β-Al_5FeSi. The introduction of the Cu-rich buffer layers facilitates the connection of Q' with the Al matrix in different orientations, giving the Q' phase more growth flexibility. In the case of the Q' nucleated at the GB, the Al matrix is shifted one Al unit cell diagonal (along <110>Al) as compared to the normal orientation. Interestingly, some Q' unit cell Si corners inside the precipitate, marked by arrows, are unusually bright, indicating Cu enrichment. In the case of the Q' nucleated on the β-Al$_5$FeSi, the Al matrix has a 30° rotation with respect to the normal orientation as shown in the supplementary material. Fig. 9 (b) was flipped and rotated to have the same precipitate orientation as the normal interface image.

The average grain sizes of as-extruded 0.2 Fe and 1 Fe are 134.8 and 33.8 μm, respectively, estimated by optical microscope. The nucleation sites at grain boundaries increase with the refining grain size of the 1 Fe alloy. Although the precipitation hardening in the matrix of the 1 Fe alloy is reduced compared to the 0.2 Fe alloy as seen in in Table 2, diverse nucleation sites for hardening precipitates i.e. grain boundaries and β-Al$_5$FeSi particles during aging are higher in numbers. Solute elements and vacancies tend to diffuse toward grain boundaries and interfaces of large particles such as β-Al$_5$FeSi, during cooling and aging. Therefore, higher density of grain boundaries and fragmented β-Al$_5$FeSi particles in this alloy provides high-diffusivity paths for vacancies. We suggest that this is the reason for the improved mechanical properties of the 1 Fe alloy.

3.3 Age-hardening of T5 treated 1 Fe alloys

The kinetics of precipitate formation are decelerated by the lack of solution heat treatment in the T5 condition, as shown in Fig. 1 (b). It is due to the low vacancy concentration and supersaturation of solute atoms in the material from slow air cooling and long NA after extrusion. TEM micrographs of the T5 treated 1 Fe alloy aged for 8 h are shown in Fig. 10. Fine dots are detected with BF (a) and dark-field (DF) (b) TEM. The selected area diffraction pattern (c) shows diffuse dots, which are a signature of atomic clustering [34-35]. A HAADF-STEM image is displayed in (d), filtered by selecting the corresponding cluster spots in the FFT of the image, and using Gaussian blur in DigitalMicrograph on the IFFT image to improve the visibility of the atomic clusters. The Cu-rich clusters are extremely small and with much less structure than, for example, the clusters in the Al-Mg-Zn system [36].

Micrographs of the T5 treated 1 Fe alloy aged for 72 h are shown in Fig. 11. The microstructure contains large plate-shaped particles in addition to the fine needle-shaped precipitates similar to those found in the 72 h aged T6 condition (shown in Fig. 2 (d)). The nano-sized precipitates were investigated by HADDF-STEM to identify their crystal structure and a representative selection is shown in Fig. 12. A new type of precipitate containing Mg and Si delimited by Cu walls with $5dAl_{200}$ separation is shown in (a). Two examples of β'' phase with Cu segregation at interfaces are presented in (b-c). Strong Cu enrichment of the Si_3/Al interior sites [37] is observed in (c). Cu capsules with Mg-Si-Cu phase interiors are presented in (d) and (e). In (d) the interfaces consist of Cu walls, while the precipitate in (e) has more irregular interfaces. The interface at the lower precipitate side in this case incorporates the same triangular Cu structure also observed at the Q'-Al interface in Fig. 7 (e). Therefore, two types of segregation were identified. The most common one is the Cu wall and the other one is the new triangular configuration observed in connection to the Q' coherent interface. L phases with asymmetric and symmetric structures are identified in (f-g), respectively. The larger plate-shaped particles are identified as θ' and pure Si (h-i). The size of the hybrid precipitates remains quite smaller as compared to the θ' and Si precipitates even during prolonged aging. The θ' phase and Si precipitates, which are nucleated by clusters formed from room temperature storage and excess Si content [8, 12, 38], are relatively coarse after 72 h aging.

During the early aging, the T6 state has its lowest hardness as all solute elements are in solution, while T5 retains clusters and some Q' phases nucleated on GBs and β-Al_5FeSi. Extruded samples were cooled down from semi solid temperature. Natural aging was conducted for approximately six months. Those offer the formation of clusters. Fine Cu clusters are identified in T5 treated 1 Fe aged at 8 h (Fig. 10). It is deduced that rapid coarsening may occurs due to the dissolution and remaining of atomic clusters.

In addition, dislocations generated from the semi solid extrusion affects the kinetic of precipitates. J. Hu et. al [39] concluded that the formation of precipitates of Al-Mg-Si alloys was accelerated by a high number density of dislocations using an extrusion forming process. More nucleation sites were provided with deformed materials compared to undeformed one. The nucleation of β'' phase prefer to form in matrix while the nucleation of β' favors to form at dislocations when a certain dislocation induced [40]. Thus, T5 treated alloys are forced to offer numerous nucleation sites from dislocations by the D-SSE process though there was lower SSSS. The precipitate microstructure of Al-Cu-Mg-Si alloys is affected by a combination of dislocations and natural aging [41]. The dislocations formed from the D-SSE aid in the formation of Q' phase [36, 42]. The high density of disordered and fine precipitates with good thermal stability observed in the present work is probably due to Cu encapsulation of the Mg-Si phases, preventing their growth [43]. Based on the initial hardness drop in the T5 treatment it is deduced that part of the clusters formed during natural aging dissolve initially, while a second wave of cluster precipitation takes place during longer aging time, until peak hardness. At longer aging times (during overaging) no clusters are observed as the microstructure in this case consists of Cu-encapsulated needles/laths. It is debatable whether clusters formed from natural aging and those from artificial aging are similar. Clearly, the thermo mechanical process and natural aging in the T5 treatment give a favorable combination of high strength and good thermal stability in this condition. The HAADF-STEM technique has proven very valuable for investigating the crystal structure of hybrid phases i.e. hybrid β'', Q', L, Cu capsule in Al-Si-Cu-Mg(-Fe) alloys. This technique allows insights of precipitation behavior and provides information of hybrid phases containing Cu.

4. Conclusions

Semisolid extruded profiles were artificially aged with T6 and T5 heat treatments. Solution heat treatment and aging (T6) led to the formation of needle/lath metastable precipitates in the matrix at both peak hardness and overaged conditions. Their number densities were slightly reduced in the 1 Fe alloy, as compared to the 0.2 Fe. However, the 1 Fe alloy produced a higher hardness due to the additional contribution from precipitates nucleated on grain boundaries and on fragmented β-Al_5FeSi phases. Interestingly, only atomic clusters were observed up to peak hardness in the T5 treatment despite an initial hardness drop. ~~However,~~ Metastable needle/lath precipitates were observed in the overaged conditions of this heat treatment, together with large Si plates and θ' particles.

Most of the needle/lath metastable precipitates in the T6 treatment consist of disordered β'', L/C type with Cu walls at their interfaces, which can be described as 'Cu capsule' types. ~~A recently discovered precipitate type with 6dAl_{200} between the Cu walls was also found. With overaging Q' was observed in addition to the aforementioned phases, but with the main difference that most of the precipitates are completely encapsulated by Cu walls or Cu-enriched interfaces. This was also found in the overaged conditions of the T5 treatment.~~ Two new coherent Q'-phase interface along <510>Al have been found, as well as a new type of precipitate consisting of a Mg-Si core delimited by Cu walls separated by 5dAl_{200}. The new interfaces offer the Q' phase greater flexibility for nucleation and growth by introducing a buffer layer of Cu-rich atomic columns between the Q' unit cells and the Al matrix.

Acknowledgements

The international collaboration was made possible through an INTPART project from the Norwegian Research Council, project number 249698. The (S)TEM work was conducted on the NORTEM infrastructure at the TEM Gemini Centre, Trondheim, project number 197405.

Data availability

The TEM images presented in this work are given in raw/processed form. The raw/processed scanning diffraction data required to reproduce these findings cannot be shared at this time as the data also forms part of ongoing study.

References

1. Z. Zhang, H. Tezuka, E. Kobayashi T. Sato, Effects of the Mn/Fe ratio and cooling rate on the modification of Fe intermetallic compounds in cast A356 based alloy with different Fe contents, Mater. Trans. 54 (8) (2013) 1484-1490, https://doi.org/10.2320/matertrans.F-M2013808.
2. Q.G. Wang, Microstructural effects on the tensile and fracture behavior of aluminum casting alloys A356/357, Metall. and Mat. Trans. A 34 (2003), 2887-2899, https://doi.org/10.1007/s11661-003-0189-7.
3. X. Cao, J. Campbell, Morphology of β-Al5FeSi phase in Al-Si cast alloys, Mater. Trans. 47 (5) (2006) 1303–1312, https://doi.org/10.2320/matertrans.27.1303.
4. T. Sato, T. Tani and T. Aoki, Characteristic local elongation of high Fe-contatining aluminum alloys produced by a deformation-semisolid-forming process, Journal of Japan Institute of Light Metals 68 (2018) 77-78, https://doi.org/10.2464/jilm.68.77.
5. C. Phongphisutthinan, H. Tezuka, and T. Sato, Caliber rolling process and mechanical properties of high Fe-containing Al–Mg–Si alloys, Mat. Trans. 53 (2012) 885-892, https://doi.org/10.2320/matertrans.MBW201121.
6. T. Sato, H. Tezuka, A new deformation-semi-solid casting process of highly concentrated Fe containing Al-Si-Cu-Fe cast alloys, Solid State Phenomena. 116–117 (2006) 247–250, https://doi.org/10.4028/www.scientific.net/SSP.116-117.247.
7. F.J. Tavitas-Medrano, A.M.A. Mohamed, J.E. Gruzleski, F.H. Samuel, H.W. Doty, Precipitation-hardening in cast Al-Si-Cu-Mg alloys, J. Mater. Sci. 45 (2010) 641-651, https://doi.org/10.1007/s10853-009-3978-6.
8. S.J. Andersen, C.D. Marioara, J. Friis, S. Wenner, R. Holmestad, Precipitates in aluminum alloys, Advances in Physics: X. 3, (2018) 790-813, https://doi.org/10.1080/23746149.2018.1479984.
9. C.D. Marioara, S.J. Andersen, T.N. Stene, H. Hasting, J. Walmsley, A.T.J. Van Helvoort, R. Holmestad, The effect of Cu on precipitation in Al-Mg-Si alloys, Philos. Mag. 87 (2007) 3385–3413, https://doi.org/10.1080/14786430701287377.
10. K. Matsuda, D. Teguri, T. Sato, Y. Uetani, S. Ikeno, Cu segregation around metastable phase in Al-Mg-Si

alloy with Cu, Mater. Trans. 48(5) (2007) 967-974, https://doi.org/10/2320/matertrans.48.967.

11. F.W. Gayle, M. Goodway, Science 266 (issue 5187) (1994) 1015-1017, https://doi.org/10.1126/science.266.5187.1015.

12. C.D. Marioara, J. Friis, E. Hersent, A. Oskarsson, A transmission electron microscopy study of precipitate phases that form during operation in a heat exchanger alloy, Mater. Charact. 149 (2019) 218-225, https://doi.org/10.1016/j.matchar.2019.01.035.

13. Q. Xiao, H. Liu, D. Yi, D. Yin, Y. Chen, Y. Zhang, B. Wang, Effect of Cu content on precipitation and age-hardening behavior in Al-Mg-Si-xCu alloys, J. Alloy. Comp. 695 (2017) 1005-1013, https://doi.org/10.1016/ j.jallcom.com.2016.10.221.

14. D.J. Charkrabarti, D.E. Laughlin, Phase relations and precipitation in Al-Mg-Si alloys with Cu additions, Prog. Mater. Sci. 49, (2004) 389-410, https://doi.org/10.1016/s0079-6425(03)00031-8

15. M. Gazizov, C.D. Marioara, J. Friis, S. Wenner, R. Holmestad, R. Kaibyshev, Precipitation behavior in an Al-Cu-Mg-Si alloy during ageing, Mat. Sci. Eng. A 767 (2019) 138369, https://doi.org/10.1016/j.msea.2019.138369.

16. S. Wenner, C.D. Marioara, S.J. Amdersem. M. Ervik, R. Holmestad, A hybrid aluminum alloy and its zoo of interacting nano-precipitates, Mater. Charact. 106 (2015) 226-231, https://doi.org/10.1016/j.matchar.2015.06.002.

17. L. Ding, A. Orekhov, Y. Weng, Z. Jia, H. Idrissi, D. Schryvers, S. Muraishi, L. Hao, Q. Liu, Study of the Q' (Q)-phase precipitation in Al-Mg-Si-Cu alloys by quantification of atomic-resolution transmission electron microscopy images and atom probe tomography , J. Mater. Sci. 54 (2019) 7943-7952, https://doi.org/10.1007/s10853-019-03427-6.

18. L. Ding, Z. Jia, J. Nie, Y. Weng, L. Cao, H. Chen, X. Wu, Q. Liu, The structural and compositional evolution of precipitates in Al-Mg-Si-Cu alloy, Acta Materialia 145 (2018) 437-450, https://doi.org/10.1016/j.actamat.2017.12.036.

19. F. J. H. Ehlers, S. Wenner, S.J. Andersen, C.D. Marioara, W. Lefebvre, C.B. Boothroyd, R. Holmestad, Phase stabilization principle and precipitate-host lattice influences for Al-Mg-Si-Cu alloy precipitates, J. Mater. Sci. 49 (2014) 6413-6426, https://doi.org/10.1007/s10853-014-8371-4.

20. C.D. Marioara, S.J. Andersen, H.W. Zandbergen, R. Holmestad, The influence of alloy composition on precipitates of the Al-Mg-Si system, Metall. Mater. Trans. A, 36 (2005) 691-702, https://doi.org/10.1007/s11661-005-0185-1.

21. J. Kim, C.D. Marioara, R. Holmestad, E. Kobayashi, T. Sato, Effects of Cu and Ag additions on age-hardening behavior during multi-step aging in Al-Mg-Si alloys Mat. Sci. Eng. A 560 (2013) 154-162, https://doi.org/10.1016/j.msea.2012.09.051.
22. R.F. Egerton, Electron energy-loss spectroscopy in the electron, microscope, https://doi.org/10.1007/978-1-4419-9583-4_9.
23. K. Oh-ishi, T. Ohsuna, Inelastic mean free path measturement by STEM-EELS technique using needle-shaped specimen, Ultramicroscopy 212 (2020) 112955, https://doi.org/10.1016/j.ultramic.2020.112955.
24. S. Ahn, S. Pathan, J. Koo, C. Baeg, C. Jeong, H. Son, Y. Kim, K. Lee and S Hong, Enhancement of the mechanical properties in Al-Si-Cu-Fe-Mg alloys with various processing parameters, Materials, 11 (2018) 2150, https://doi.org/10.3390/ma11112150.
25. J. Mathew, G. Remy, M.A. Williams, F. Tang and P. Srirangam, Effect of Fe intermetallics on microstructure and properties of Al-7Si alloys, JOM 71, (2019) 4362-4369, https://doi.org/10.1007/s11837-019-03444-5.
26. L. Kovarik, S.A. Court, H.L. Fraser, M.J. Mills, GPB zones and composite GPB/GPB zones in Al-Cu-Mg alloys, Acta Mater. 56 (2008) 4804-4815, https://doi.org/10.1016/j.actamat.2008.05.042.
27. M. Mihara, C.D. Marioara, S.J. Andersen, R. Holmestad, E. Kobayashi, T. Sato, Precipitation in an Al-Cu-Mg alloy and the effect of a low amount of Ag, Mater. Sci. Eng. A 658 (2016) 91-98, https://doi.org/10.1016/j.msea.2016.01.087.
28. T. Saito, C.D. Marioara, S.J. Andersen, W. Lefebvre, R. Holmestad, Aberration-corrected HAADF-STEM investigations of precipitate structures in Al-Mg-Si alloys with low Cu additions, Philos. l Mag. 94(5) (2014) 520-530, https://doi.org/10.1080/14786435.2013.857051.
29. E.A. Mørtsell, S.J. Andersen, J. Friis, C.D. Marioara, R. Holmestad, Atomistic details of precipitates in lean Al-Mg-Si alloys with trace additions of Ag and Ge studied by HAADF-STEM and DFT, Philos. Mag. 97 (2017) 851-866, https://doi.org/10.1080/14786435.2017.1281461.
30. S.J. Andersen, C.D. Marioara, J. Friis, R. Bjørge, Q. Du, I.G. Ringdalen, S. Wenner, E.A. Mørtsell, R. Holmestad, T. Saito, J. Røyset, O. Reiso, Directionality and column arrangement principles of precipitates in Al-Mg-Si-(Cu) and Al-Mg-Cu linked to line defect in Al, Materials Science Forum 877 (2016) 461-470, https://doi.org/10.4028/www.scientific.net/MSF.877.461.
31. E.A. Mørtsell, F. Qian, C.D. Marioara, Y. Li, Precipitation in an A356 foundry alloy with Cu additions – A transmission electron microscopy study, J. Alloy. Comp. 785 (2019) 1106-1114,

https://doi.org/10.1016/j.jallcom.com.2019.01.229.

32. A. Lervik, C.D. Marioara, M. Kadanik, J.C. Walmsley, B. Milkereit, R. Holmestad, Precipitation in an extruded AA7003 aluminum alloy: Observations of 6xxx-type hardening phases, Mater. Des. 186 (2020) 108204, https://doi.org/10.1016/j.matdes.2019.108204.

33. J.A. Taylor, Iron-containing intermetallic phases in Al-Si based casting alloys, Procedia Mater. Sci. 1 (2012) 19-33, https://doi.org/10.1016/j.mspro.2012.06.004.

34. K. Matsuda, A. Kawai, K. Watanabe, S. Lee, C.D. Marioara, S. Wenner, K. Nishimura, T. Matsuzaki, N. Numomura, T. Sato, R. Holmestad, S. Ikeno, Extra electron diffraction spots caused by fine precipitates formed at the early stage of aging in Al-Mg-X (X=Si, Ge, Zn)-Cu alloys, Mater. Trans. 58 (2017) 167-175, https://doi.org/10.2320/matertrans.L-M2016839.

35. R.S. Yassar, D.P. Field, H. Weiland, The effect of predeformation on the and precipitates and the role of Q' phase in an Al-Mg-Si alloy; AA6022, Scr. Mater. 53 (2005) 299-303, https://doi.org/10.1016/j.scriptamat.2005.04.013.

36. K. Matsumoto, Y. Aruga, H. Tsuneishi, H. Iwai, M. Mizuno, H. Araki, Effects of precipitation state on serrated flow in Al-Mg(-Zn) alloy, Mater. Trans. 57(7) 2016 1101-1108, https://doi.org/10.2320/matertrans.L-M2016814.

37. T. Saito, E.A. Mørtsell, S. Wenner, C.D. Marioara, S.J. Andersen, J. Friis, K. Matsuda, R. Holmestad, Atomic structures of precipitates in Al-Mg-Si alloys with small additions of other elements, Adv. Eng. Mater. 20 (2018) 1800125, https://doi.org/10.1002/adem.201800125.

38. D.G. Eskin, Hardening and precipitation in the Al-Cu-Mg-Si alloying system, Materials Science Forum 396-402 (2002) 917-922, https://doi.org/10.4028/www.scientific.net/MSF.396-402.917.

39. J. Hu, W. Zhang, D. Fu, J. Teng and H. Zhang, Improvement of the mechanical properties of Al-Mg-Si alloys with nano-scale precipitates after repetitive continuous extrusion forming and T8 tempering, Mater. Res. Technol. 8 (6) (2019) 5950-5960, https://doi.org/10.1016/j.jmrt.2019.09.070.

40. O.R. Myhr, O. Grong and C. Schafer, An extended age-hardening model for Al-Mg-Si alloys incorporating the room-temperature storage and cold deformation process stages, Metall. Mater. Trans. A 46A (2015) 6018-6039, https://doi.org/10.1017/s11661-015-3175-y.

41. E. Thronsen, C.D. Marioara, J.K. Sunde, K. Minakuchi, T. Kastumi, I. Erga, S.J. Andersen, J. Friis, K. Marthinsen, K. Matsuda, R. Holmestad, Mat. Des. 186 (2020) 108203, https://doi.org/10.1016/j.matdes.2019.108203.

42. E. Sjolander, S. Seifeddine, The heat treatment of Al-Si-Cu-Mg casting alloys, J. Mat. Pro. Tech. 210 (2010) 1249-1259, https://doi.org/10.1016/j.matprotec.2010.03.020.

43. C.D. Marioara, S.J. Andersen, J. Røyset, O. Reiso, S. Gulbrandsen-dahl, T. Nicolaisen, I. Opheim, J.F. Helgaker, R. Holmestad, Improving thermal stability in Cu-containing Al-Mg-Si alloys by precipitate optimization, Metall. Mater. Trans. A, 45A (2014) 2938-2949, https://doi.org/10.1007/s11661-014-2250-0.

Table 1 Chemical composition of experimental alloys (wt.%).

Alloy	Si	Cu	Mg	Fe	Al
0.2 Fe	4.44	1.09	0.39	0.15	Bal.
1 Fe	4.47	0.98	0.35	1.02	Bal.

Table 2 Statistic results of precipitates in T6 treated alloys.

Material	Cross section [nm^2]	Needle length [nm]	Number density [#/um^3]	Volume fraction [%]
0.2 Fe 6 h	2.9 ±0.2	16.2 ± 10	2303.2 ± 523.8	(0.1, 0.13)
0.2 Fe 72 h	3.5 ± 0.4	30.8 ± 5.5	1236.6 ± 184.3	(0.18, 0.33)
1 Fe 6 h	3.3 ± 0.3	13.3 ± 2.2	1744.0 ± 265.5	(0.07, 0.12)
1 Fe 72 h	4.4 ± 0.8	40 ± 4.1	687.0 ± 240.9	(0.29, 0.38)

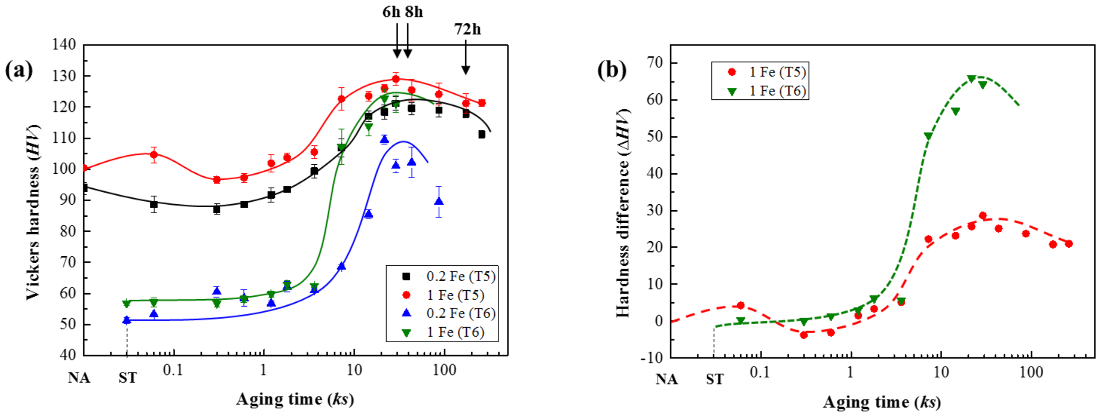

Fig. 1 (a) Age-hardening curves of T5 and T6 treated 0.2 Fe and 1 Fe alloys and (b) hardness difference of T5 and T6 treated 1 Fe alloys.

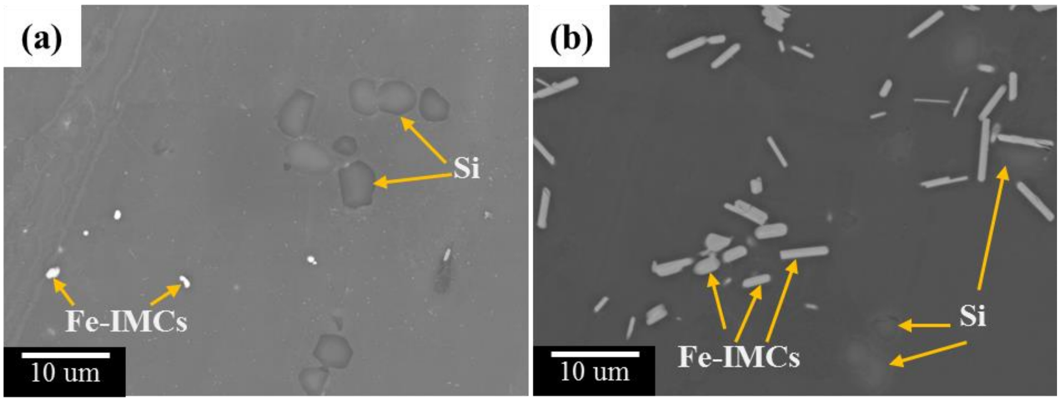

Fig. 2 SEM images of as-extruded samples (before T5/T6 aging); (a) as-extruded 0.2 Fe and (b) as-extruded 1 Fe.

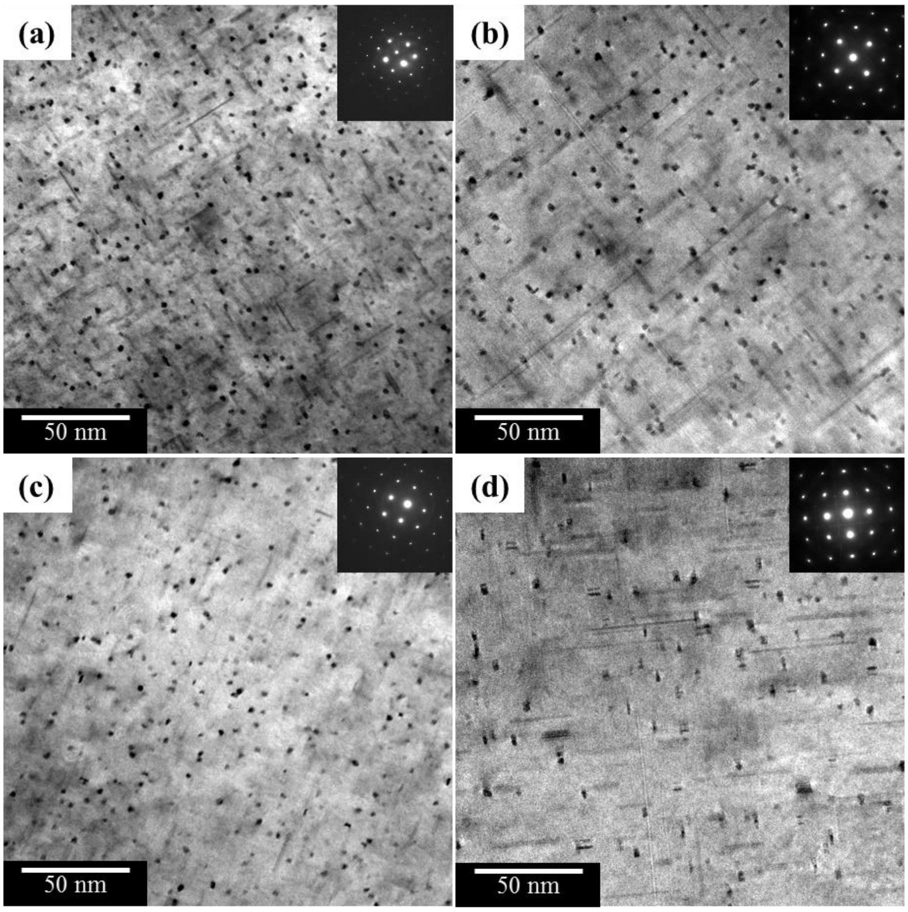

Fig. 3 Overview bright-field TEM images of T6 treated alloys for different times; (a) 0.2 Fe for 6 h,(b) for 72 h ,(c) 1 Fe for 6 h, (d) for 72 h used to determine the precipitate statistics.

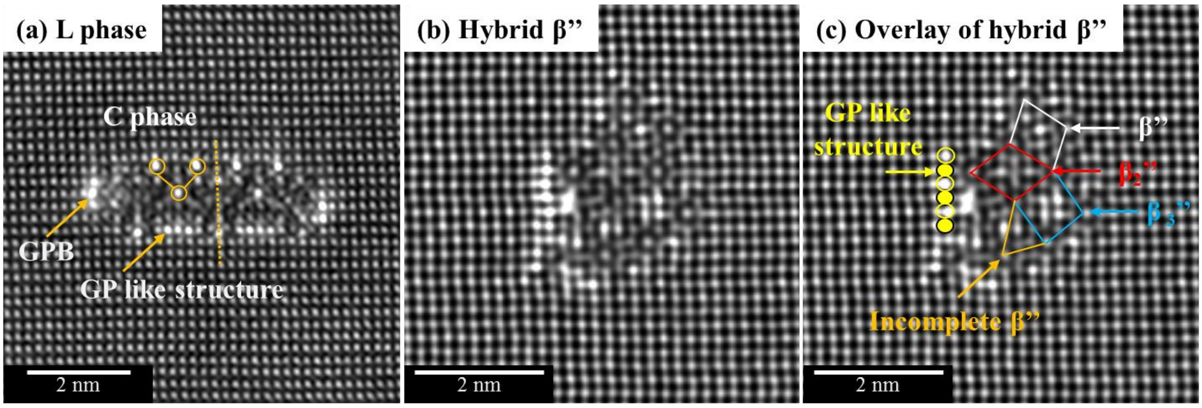

Fig. 4 STEM images of T6 treated 0.2 Fe alloy aged for 6 h; (a) L and (b) β" phase mixed with GP like structure. The location of the GPB unit and GP-like structure (Cu wall) are indicated by arrows in a). Three columns delimiting a local C-phase configuration are connected by full line, and a mirror plane is indicated by a dotted line. c) is an overlay of the image in b) showing the location of a GP-like structure and the different types of β" that comprise this precipitate.

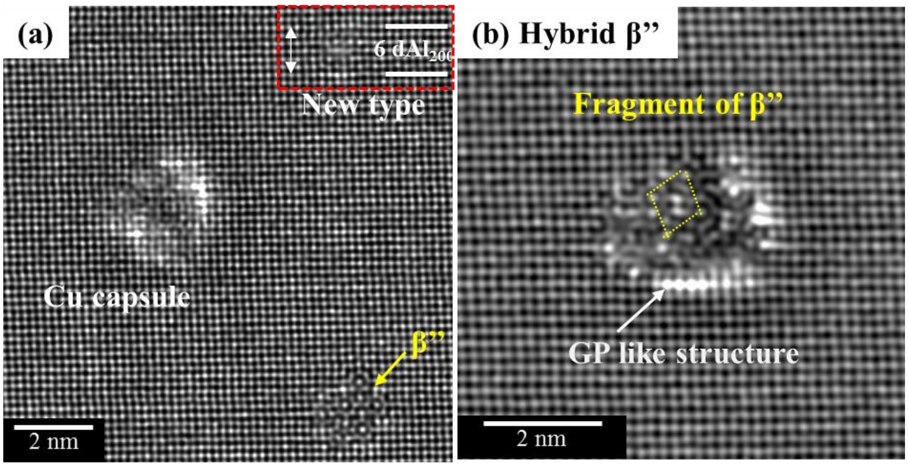

Fig. 5 STEM images of T6 treated 1 Fe alloy aged for 6 h; (a) Cu capsule, new type precipitate with Cu walls separated by 6d Al_{200} and β'' phase, (b) hybrid β'' phase.

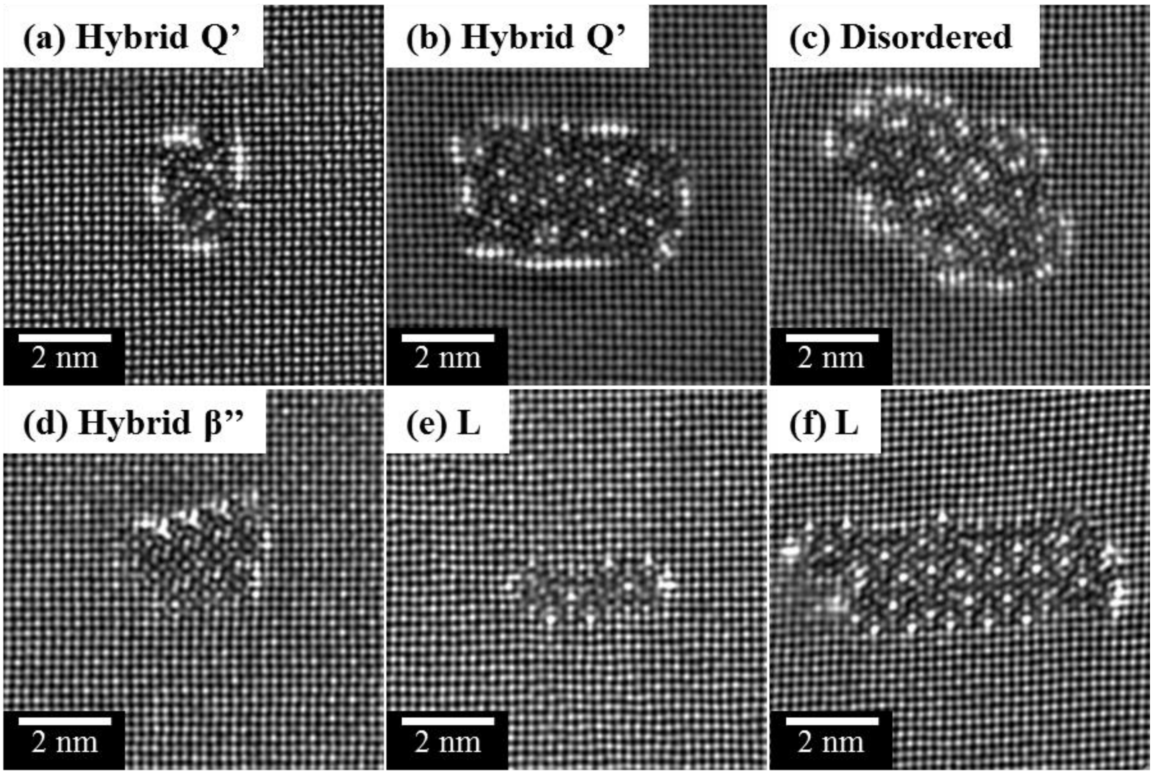

Fig 6 HAADF-STEM images of T6 treated 1 Fe alloy aged for 72 h; (a-b) hybrid Q' phases, (c) disordered with Cu walls, (d) hybrid β", (e-f) L phases.

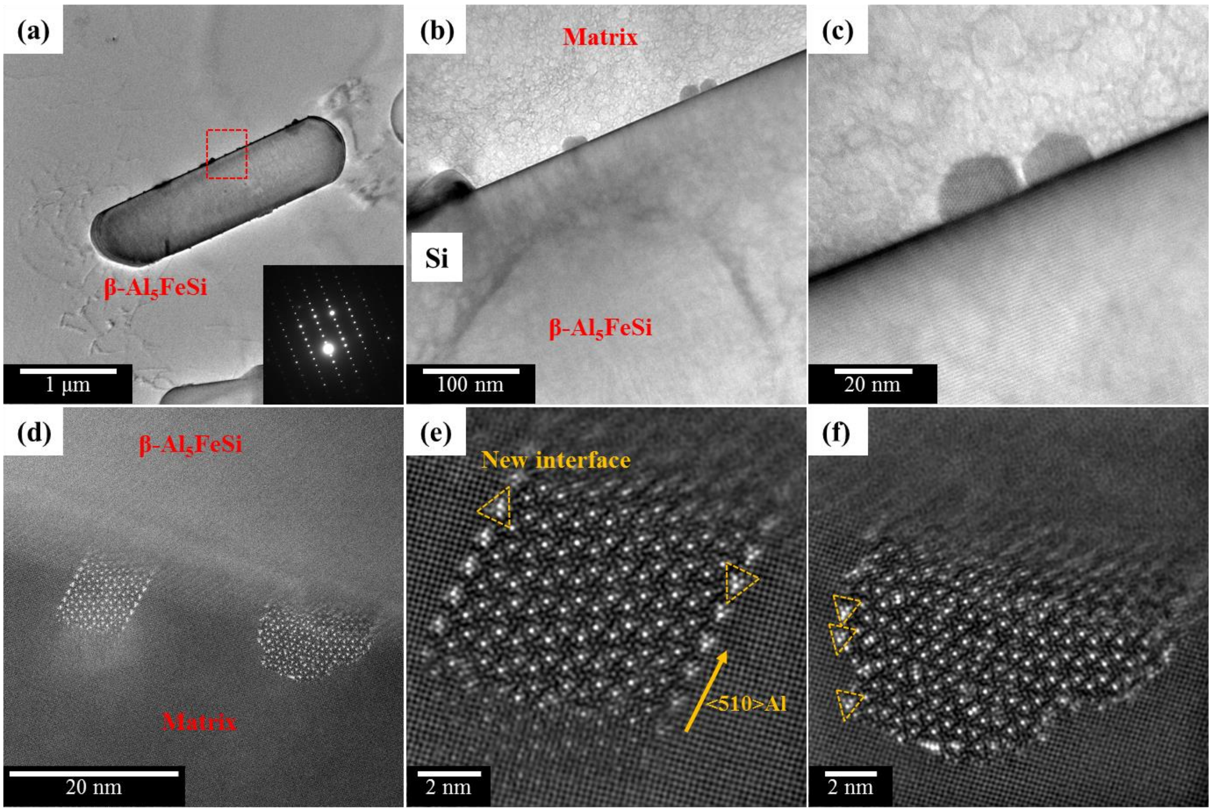

Fig. 7 (S)TEM images of the T6 treated 1 Fe alloy aged for 8 h; (a) BF-TEM, β-Al_5FeSi particle, (b-c) BF-TEM, enlarged interface of (a) image, (d-f) HAADF-STEM images of Q' phases obtained at different locations on the boundary of β-Al_5FeSi. A new coherent Q' interface with the Al matrix along <510> is found, and its distinctive triangular appearance is marked in e). Structural units of this interface (triangles) are sporadically observed in the case of a less coherent Q' interface in f).

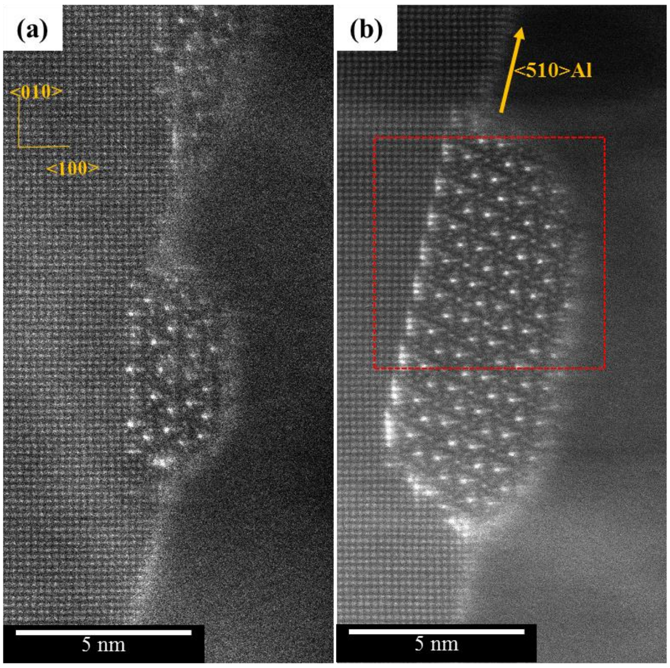

Fig. 8 (a-b) HAADF-STEM images of grain boundary precipitates in the T6 treated 1 Fe alloy aged for 6 h. For the Q' precipitates in b), a previously unreported coherent interface is identified, consisting of local GP-like structures with 1.04 nm periodicity along <510>Al, marked by arrows.

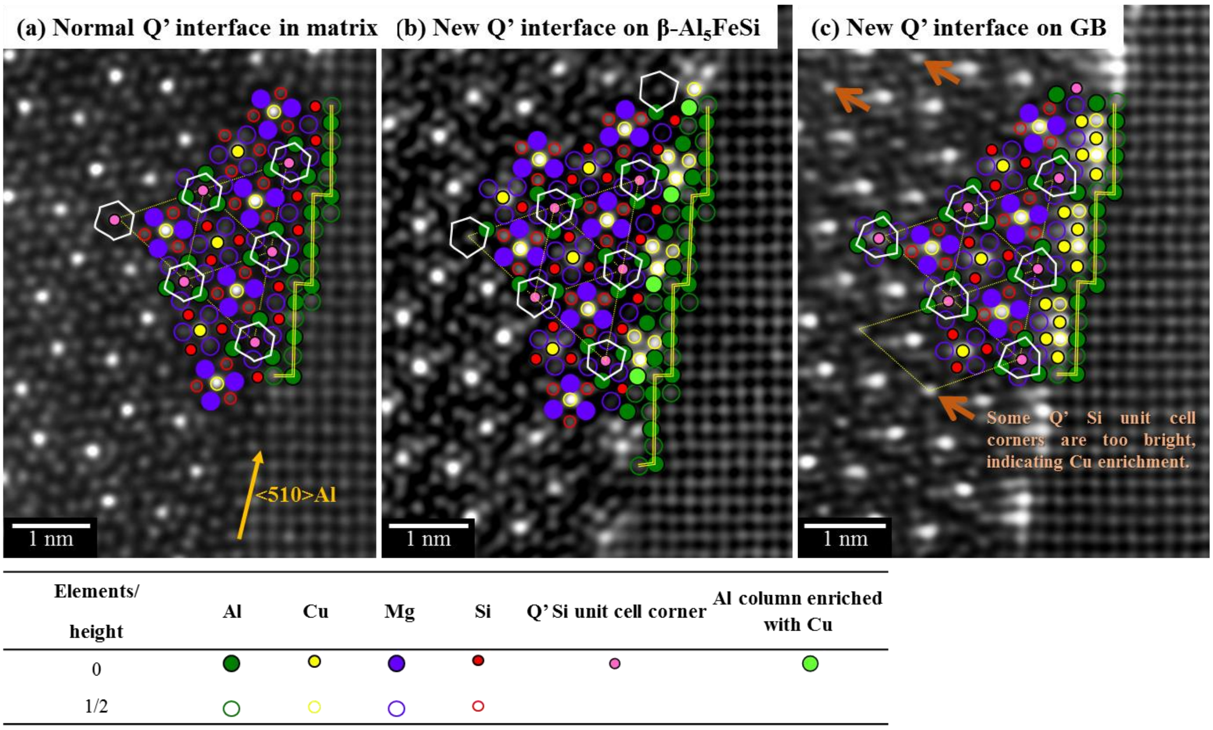

Fig. 9 Atomic overlay of Q' phases with different coherent interfaces with the Al matrix along <510>Al; (a) normal Q' interface [12], (b) new interface of Q' nucleated on a β-Al_5FeSi particle from Fig. 7 (e) and (c) new interface of Q' nucleated on a GB from Fig. 8 (b). The flipped and rotated Fig. 9 (b) is presented in the supplementary material. To facilitate the comparison between the images, the rings of near neighbor atomic columns with the unit cell corners are connected by white lines, and the unit cell corners by dotted yellow lines. The matrix Al in contact with the Q' phases are indicated by yellow double lines.

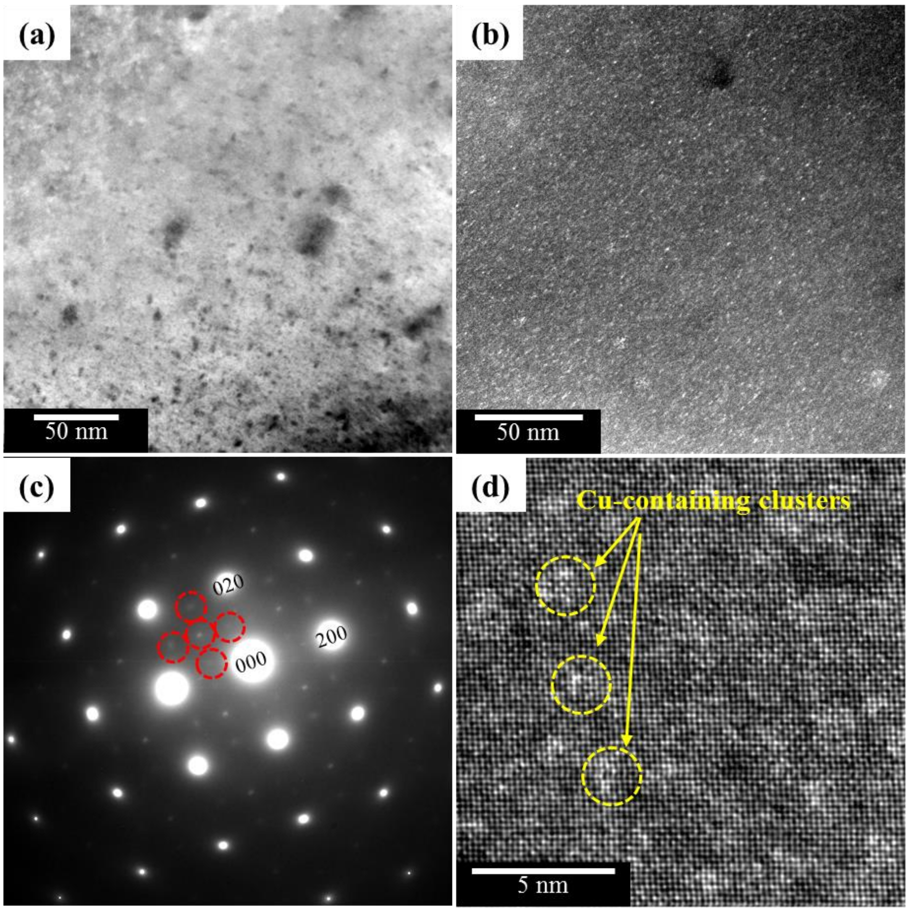

Fig. 10 TEM images of the T5 treated 1 Fe alloy aged for 8 h; (a) BF-TEM, (b) DF-TEM, (c) selected area diffraction pattern, (d) Gaussian blur filtered HAADF-STEM image. Bright spots indicate the presence of Cu-containing atomic clusters.

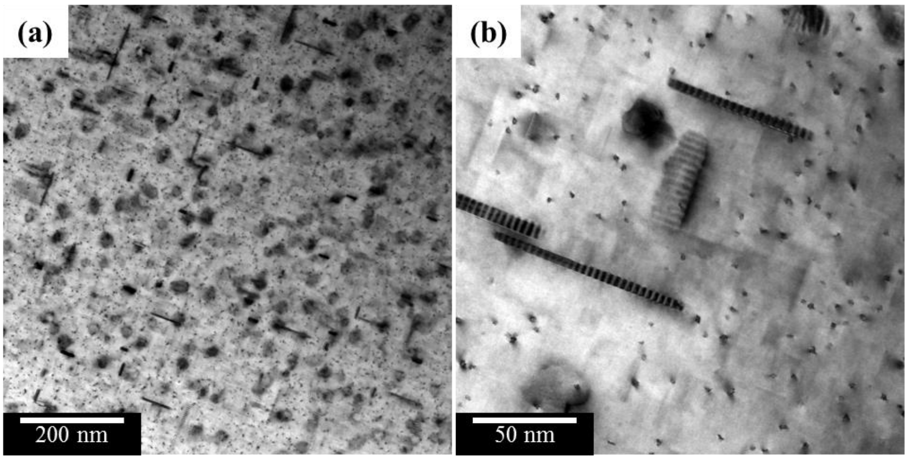

Fig. 11 BF-TEM images of the T5 treated 1 Fe alloy aged for 72 h; (a) low and (b) high magnification.

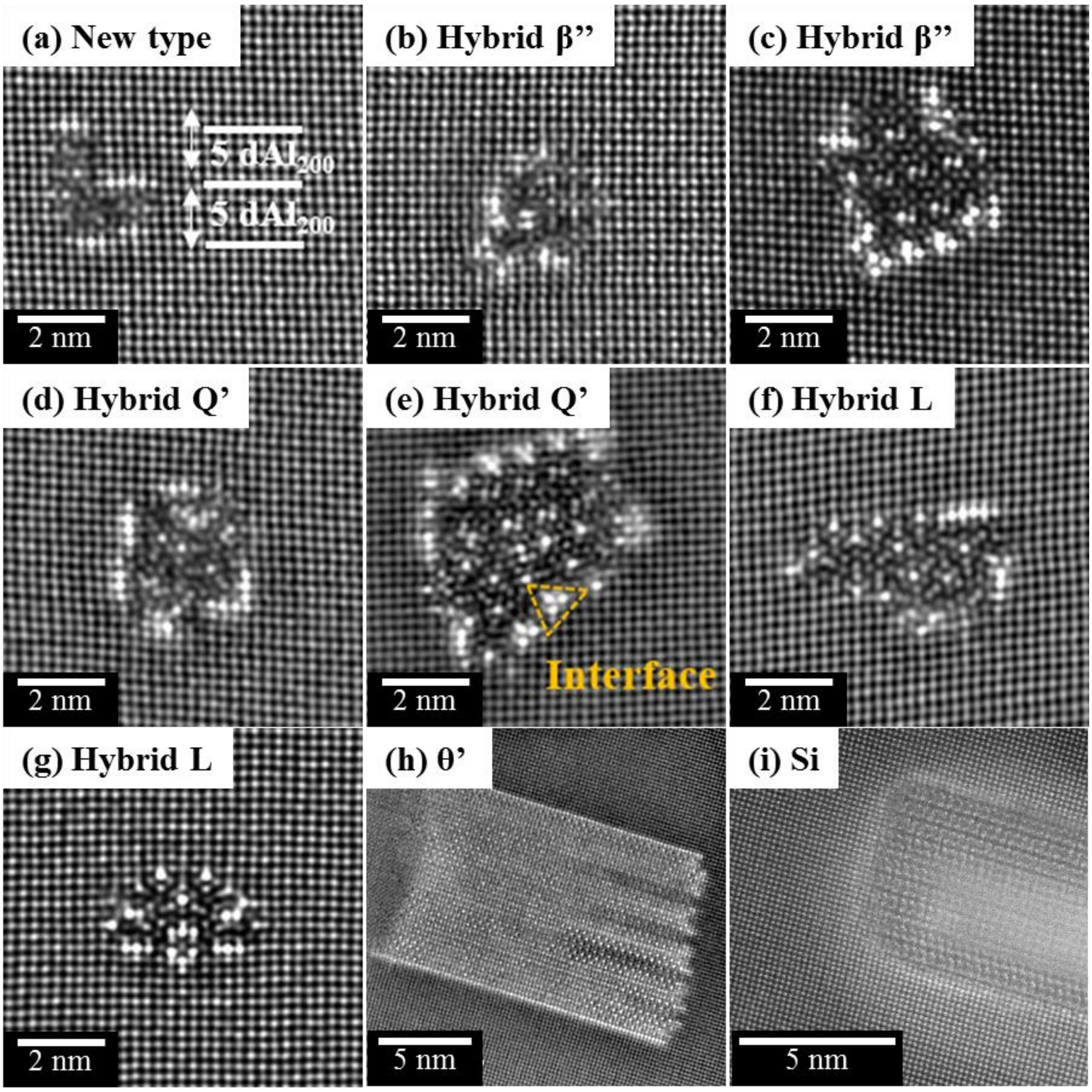

Fig. 12 HAADF-STEM images of the T5 treated 1 Fe alloy aged for 72 h; (a) new type of precipitate, (b-c) hybrid β'', (d-e) disordered/hybrid Q' with Cu walls (d) or with the new periodic Cu-containing interface along <510>Al (e), (f-g) hybrid L, (h), θ', (i) Si plate.

Supplementary material

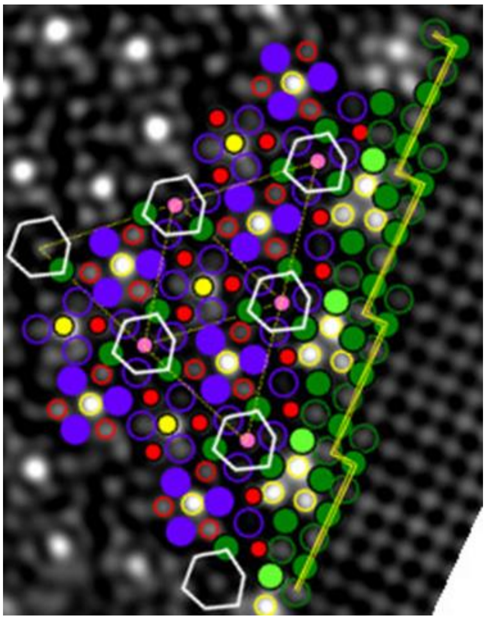

Fig. The Fig 9 (b) image flipped and rotated is provided to have the same precipitate orientation as in the normal interface image. The new interface allows the Q' precipitate to connect to the Al matrix in a different orientation.